

# Boundary-induced nucleation control: A theoretical perspective

Oleg Buller<sup>1,\*</sup>, Hong Wang<sup>2</sup>, Wenchong Wang<sup>2</sup>, Lifeng Chi<sup>2,3</sup>, and Andreas Heuer<sup>1</sup>

<sup>1</sup> Institute for Physical Chemistry, University of Münster, Correnstr. 28/30, 48149 Münster, Germany

<sup>2</sup> Physikalisches Institut und Center for Nanotechnology (CeNTech),  
University of Münster, 48149 Münster, Germany and

<sup>3</sup> Jiangsu Key Laboratory for Carbon-based Functional Materials & Devices Collaborative,  
Institute of Functional Nano & Soft Materials (FUNSOM) and  
Collaborative Innovation Center of Suzhou Nano Science and Technology,  
Soochow University, Suzhou 215123, P. R. China

The pre-patterning of a substrate to create energetically more attractive or repulsive regions allows one to generate a variety of structures in physical vapor deposition experiments. A particular interesting structure is generated if the energetically attractive region is forming a rectangular grid. For specific combinations of the particle flux, the substrate temperature and the lattice size it is possible to generate exactly one cluster per cell, giving rise to nucleation control. Here, we show that the experimental observations of nucleation control can be very well understood from a theoretical perspective. For this purpose we perform, on the one hand, kinetic Monte Carlo simulations and, on the other hand, use analytical scaling arguments to rationalize the observed behavior. For several observables, characterizing nucleation control, a very good agreement is found between experiment and theory. This underlines the generality of the presented mechanism to control the deposition of material by manipulation of the direct environment.

Keywords: Physical vapor deposition, Nucleation control, Surface diffusion, Aggregation, Mesoscopic scale

## I. INTRODUCTION

With physical vapor deposition (PVD) material can be condensed extensively onto a substrate, yielding films with desired thickness on the desired length scales [1, 2]. Atoms and molecules, also as multiple component systems, can be deposited in this way.

During the deposition the nucleation process is of major importance, therefore a critical number of particles, i.e. atoms or molecules, has to come together to form stable clusters [3, 4]. Before nucleation, on a homogeneous substrate the ad-atom density is uniform and increases linearly, in the scope of a mean-field description. The location of the first nucleus is totally random and caused by local ad-atom density fluctuations, afterwards the nucleation site becomes an absorber for the ad-atoms on the surface.

In order to place material heterogeneously on a desired position, the method of template-directed nucleation was introduced [5–10]. Here, the substrate is first chemically pre-patterned with a material, which for the deposited particles is energetically more attractive than the substrate. This procedure is typically performed by lithographic methods and applied on the (high) nano and micrometer scale [8]. Within a specific range of  $D/F$ , where  $D$  is the surface diffusion coefficient and  $F$  the particle flux of the depositing material, nucleation takes place only on the pre-defined positions, i.e. on the pre-pattern. This configuration corresponds to the equilibrium state of the system and is realized in the limit of small flux.

In a different way the "pre-patterning" can be created by Moire structures, for instance by having a monolayer of graphene on a transition metal substrate [11, 12].

Through the mismatch of lattices a periodically modulated structure is created, with a periodic variation of the binding- and transition energies on the graphene layer. A regular formation of (nano-) clusters in the sub-monolayer regime can be obtained by thermodynamic and kinetic effects [5], due to the heterogeneous substrate field structure. In this context this process is often referred by the term directed self-assembly.

The detailed mechanisms on the surface during PVD are rather complex [13, 14] and cover different time and space scales, from typical atomic vibrations ( $10^{-13}$  s) to growth processes on the mesoscopic scale with a duration of minutes or hours. In order to overcome this complexity and focus on key relations and mechanisms of the growth process, mean-field and coarse-grained approaches were introduced, which are formulated on the time scale of the transition processes. With the mean-field rate equations, describing the ad-atom and island densities with coupled ordinary differential equations, basic scaling relations of deposition growth can be elucidated [3, 4, 15, 16]. In order to capture the spatial resolution, stochastic/kinetic Monte Carlo methods are very powerful [17–20]. In this context there also exist hybrid models [21, 22] that combine the mean-field with the atomistic perspective. Other related approaches are phase-field models [23], geometry based simulations [24] or the Quasicontinuum Monte Carlo [25]. The success of these methods lies in describing accurately the main aspects of the structural surface growth during PVD, namely the diffusion and nucleation processes.

In this paper we deal with a nucleation control method where the nucleation site is spatially well-defined but which does not rely on the presence of a pre-pattern at this location. Rather the spatial position is controlled through the boundaries, given by an ad-atom adsorbing grid. This method exploits the maximum of the ad-atom

\* To whom correspondence should be addressed: o.buller@wwu.de

distribution between sinks and the existence of a critical density where nucleation commences [26, 27]. In this way, very regular structures can be generated, cf. Fig. 1 left. Note, that the mechanism is kinetically driven and the central nucleus is placed directly on the substrate. In contrast to template-directed nucleation this mechanism to generate ordered structures is a non-equilibrium process, which sensitively depends on an appropriate choice of the ratio  $D/F$ , for a fixed grid size  $L$ .

The mechanism of that approach is explored based on the previous results and the model system, put forward in [26]. The quality of the used lattice kinetic Monte Carlo (KMC) model is verified through direct comparison with the experimental results for different observables which characterize properties of the nuclei and in particular the nucleation control, i.e. the presence of one nucleus *per* grid cell. Furthermore, the dependence on the external flux of this particular structure is analyzed analytically based on the mean-field rate equations; a scaling relation is derived and verified with KMC simulations. Due to the agreement of the experimental and simulation outcome as well as the analytical scaling results, we argue that the mechanism of indirect nucleation control is of general nature and can be extended to a wide variety of scenarios.

The structure of this paper is as follows. In Sect. II we recap experimental results of cluster formation followed by the simulation setup in Sect. III. Afterwards the scaling relation from mean-field rate equation approach is derived in Sect. IV and the qualitative behavior of cluster growth presented in Sect. V. Nucleation- and position control is discussed in Sect. VI. The flux dependence of the nucleation control is presented in Sect. VII, the influence of the diffusion properties and scaling of multiple islands in Sect. VIII. Finally, we conclude with a discussion of our results in Sect. IX.

## II. EXPERIMENTAL BACKGROUND

PVD methods are suited very well to deposit complex organic molecules, which are increasingly used in microelectronics, due to the functionality and efficiency they provide. Therefore, this type of molecules is of great interest from the experimental point of view [28–31]. Here we briefly refer to the experimental set up. In general the experiments are conducted in the same way as in [26].

For deposition the functional molecule N,N'-bis(1-naphthyl)-N,N'-diphenyl-1,1'-biphenyl-4,4'-diamine (NPB, a molecule widely used for organic light emitting diodes) has been used [32]. This molecule was deposited on a silica surface. To create an attractive region for the molecules, a gold grid was put on the surface by standard beam lithography. The gold grid is acting as an adsorbing environment for the central area of the squares.

In Fig. 1 a) the scanning electron microscope (SEM) images are shown of the resulting structure for a gold array distance of  $L = 4.0 \mu\text{m}$ . The flux was increased on going from left to right. In case of the lowest flux

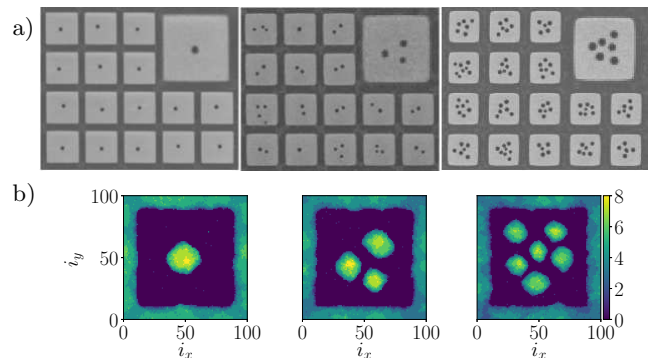


FIG. 1. a) SEM pictures of formations on a grid pre-patterned surface with  $L = 4.0 \mu\text{m}$  and flux variation  $0.042 \text{ nm min}^{-1}$ ,  $0.066 \text{ nm min}^{-1}$ ,  $0.085 \text{ nm min}^{-1}$  from left to right. The right top corner shows the magnified view of one cell, respectively. b) The height profile of a similar result from the KMC model for the grid size of  $80a$ . The flux is varied with  $5.85 \times 10^{-6}/(a^2\Delta t)$ ,  $1.40 \times 10^{-5}/(a^2\Delta t)$  and  $2.60 \times 10^{-5}/(a^2\Delta t)$  on going from left to right. The color-coding for the height is given on the right.

$F = 0.042 \text{ nm min}^{-1}$ , shown in Fig. 1 a) left, one cluster is created with a well-defined position in the center of the cell. Due to the regularity of the grid the clusters also form a regular structure, i.e. show position control. With increasing the flux, the number of clusters increases, i.e. nucleation control is no longer present. In the same way it works for other molecule types [26]. To prove the generality of the mechanism, a *solid-on-solid* model [33] is used, which only provides the basic mechanism of surface growth, i.e. a particle flux, surface diffusion and nucleation through parametrized interaction strength. Note, that within this model the deposit molecule is reduced to a point on a lattice with isotropic interaction and diffusion properties. An impression of the result from the simulations is shown in Fig. 1 b) with a similar scaling for the island number by varying the flux. The KMC model described in the following section.

## III. SIMULATION SETUP

For the simulations a lattice gas model is used on a three dimensional cubic lattice with a node distance of  $a$  as described in [26, 33]. Every lattice site  $\mathbf{i} = \{i_x, i_y, i_z\}$  can be occupied by one of the three different particle types: deposited particles  $p_i$ , substrate sites  $s_i$  and the more attractive pre-pattern sites  $g_i$  (in the experiment represented by gold). The lattice site  $\mathbf{i}$  is either filled or empty. As we are only interested in the dynamics of the deposited particles the Hamiltonian can be written as

$$H = -\varepsilon_{pp} \frac{1}{2} \sum_{\mathbf{i}, \mathbf{j}} f(r_{\mathbf{ij}}) p_i p_j - \varepsilon_{pg} \frac{1}{2} \sum_{\mathbf{i}, \mathbf{j}} f(r_{\mathbf{ij}}) p_i g_j - \varepsilon_{ps} \frac{1}{2} \sum_{\mathbf{i}, \mathbf{j}} f(r_{\mathbf{ij}}) p_i s_j, \quad (1)$$

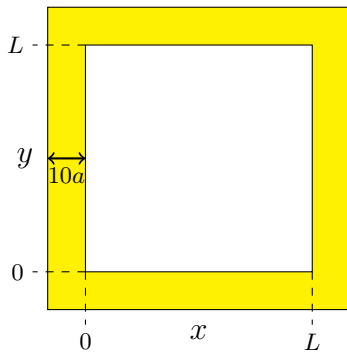


FIG. 2. Sketch of the simulation box of one cell with the energetically more attractive region in yellow and the central region of size  $L$  in white. Periodic boundary conditions are applied along the cell boundaries in  $x$  and  $y$ -direction.

where the  $\varepsilon_{xy}(x, y \in \{p, g, s\})$  are the interaction parameters. The distance scaling function  $f(r_{ij})$  depends on the distance  $r_{ij}$  between the lattice sites on  $\mathbf{i}$  and  $\mathbf{j}$  and is defined as follows:

$r_{ij}$	0.0	1.0	$\sqrt{2}$	$\sqrt{3}$	$> \sqrt{3}$
$f(r_{ij})$	0.0	1.0	1.0	0.5	0.0

The interaction range up to the third nearest neighbors (common corner) is taken into account. The interaction parameters are the same as in [26],  $\varepsilon_{pg}/k_B T = 1.3$ ,  $\varepsilon_{pp}/k_B T = 1.0$  and  $\varepsilon_{ps}/k_B T = 0.3$ , where  $k_B$  is the Boltzmann constant and  $T$  the temperature. The necessary conditions for the boundary-induced nucleation are an ad-atom absorbing environment and the island growth regime on the substrate. The absorbing environment is here realized by a energetically more attractive grid pre-pattern, i.e.  $\varepsilon_{pg} > \varepsilon_{ps}$ . In this way, the boundary of the pre-pattern represents a sink for the central region. As in this case attaching to the pre-pattern is associated with an energy gain and the detachment with an energy barrier, therefore the situation is similar to the process of aggregation to a nucleus.

One cell with an energetically more attractive environment is used as the simulation box with periodic boundary conditions in the substrate plane ( $x$ - and  $y$ - direction) as presented in Fig. 2. Simulations are done for different cell sizes  $L$  and a fixed pre-pattern stripe width of  $2 \cdot 10a$ . The substrate is composed of one layer including pre-pattern and substrate sites, which are fixed during the simulation. The diffusion activation energy on the plane and homogeneous substrate is renormalized, in order to improve the simulation speed [34, 35], by accepting every diffusion step of an ad-atom on the substrate. The simulation starts with a clean substrate. During one Monte Carlo (MC) step, corresponding to the time step  $\Delta t$ , every particle on the substrate attempts one 3D nearest-neighbor move to a new position. The jump to the new position is accepted according to the standard Metropolis criterion [36]. Despite the simplicity of the model, it provides accurate dynamics as shown by an equivalent model (except zero flux and desorption is not suppressed)

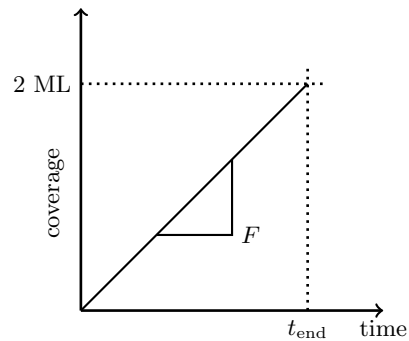


FIG. 3. Simulation time scale is directly connected to the total coverage.

for wetting film instabilities on patterned substrates [37]. Furthermore, all moves are discarded to already occupied sites or after which a particle has zero energy. In this way possible desorption processes are suppressed. After finishing the MC step,  $n$  particles are positioned on the substrate. Here,  $n \in \mathbb{N}$  is a Poissonian random number from a distribution with a mean value of  $\bar{n} \in \mathbb{R}_+$ , which is related to the average flux *via*

$$F = \frac{\bar{n}}{(A\Delta t)}. \quad (2)$$

With  $A = (L + 20a)^2$  defined as the surface area. Therefore, the flux can be varied continuously. The added particles are directly attached on a randomly chosen free location of the surface. The resulting time-dependence of the coverage (number of particles over  $A$ ) is sketched in Fig. 3.

All simulations are repeated 2000 times (representing a set of 2000 different cells) in order to obtain a good statistical description. This large number also acknowledges that the nucleation process has a significant random component which has to be appropriately averaged out for the analysis.

#### IV. THEORY OF SINGLE-CLUSTER FORMATION

In Sect. IV.2 a scaling relation is derived for the single-cluster formation with the feature of one cluster per cell  $N = 1$ , like it is presented in Fig. 1 left. Since the cluster creation process involves stochastic contributions, nucleation control is defined by the condition that on average one cluster *per* cell is present, i.e.  $\langle N \rangle = 1$  after the deposition of 2 ML. The scaling relations, to be derived below, are based on the insight about nucleation control, described in our previous work [26]. Therefore, these results are briefly summarized in Sect. IV.1 first.

##### IV.1. Existence of a critical density

Assuming the particle density distribution  $\rho(x, y, t)$ , with  $x, y \in [0, L]$  under the condition that no nucleation

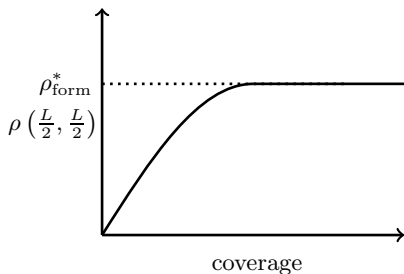


FIG. 4. Evolution of  $\rho(x = L/2, y = L/2, t)$  with coverage in the *cluster-free sub-ensemble* for a parameter set with  $\langle N \rangle = 1$ . The long-time limit of  $\rho(L/2, L/2, t)$ , denoted  $\rho^*$ , defines the value of  $\rho_{\text{form}}^*$ .

has occurred until time  $t$ , i.e. no increase of the local density due to nucleation occurs, then  $\rho(x, y, t)$  corresponds in a good approximation to the ad-atom density. Thus, the mean-field approach based on Burton-Cabrera-Frank theory can be applied for the case of complete condensation [9, 38, 39]. Applying adsorbing boundary conditions, cf. Sect. III, the stationary solution

$$\rho_{\text{stat}}(x, y) = \frac{FL^2}{D} g\left(\frac{x}{L}, \frac{y}{L}\right) \quad (3)$$

is derived, with the explicit form of function  $g(x/L, y/L)$  found in [26]. The stationary density  $\rho_{\text{stat}}(x, y)$  displays a significant maximum in the center of the cell. The density  $\rho^* \equiv \rho_{\text{stat}}(x = L/2, y = L/2)$  at this maximum is

$$\rho^* = \frac{FL^2}{D} C, \quad (4)$$

with the constant  $C = g(\frac{1}{2}, \frac{1}{2})$ . For the interesting parameter set expecting  $\langle N \rangle = 1$  a sketch of the time-dependence  $\rho(x = L/2, y = L/2, t)$  is shown in Fig. 4. Note, that in simulations only those realizations (cells) contribute to the density calculation for which until time  $t$  no nucleation process has occurred (*cluster-free sub-ensemble*). The long-time limit of  $\rho(L/2, L/2)$  in the simulations agrees very well with the analytically calculated value of  $\rho^*$ ; cf. Eq. 4. We denote this value  $\rho_{\text{form}}^* = \rho^* = \rho(L/2, L/2)$ , which is obtained for this special parameter combination with  $\langle N \rangle = 1$ . This value is of major importance when analyzing simulations with a different value of  $L$  and a fixed  $D/F$ . For smaller  $L$ , implying  $\rho^* < \rho_{\text{form}}^*$  cluster formation is strongly suppressed, i.e.  $\langle N \rangle < 1$ . In contrast, in the opposite limit many clusters start to grow as soon as  $\rho(x = L/2, y = L/2, t)$  approaches  $\rho_{\text{form}}^*$ . Thus, the stationary regime is never reached because of preceding nucleation events. As a consequence  $\rho_{\text{form}}^*$  can be interpreted as the critical density where nucleation sets in. Since the nucleation rate scales with a high power of the density (depending on the size of the critical nucleus), this observation is in agreement with mean-field nucleation theory [3, chap. 2].

As a consequence of this interpretation, it comes out that for  $\langle N \rangle = 1$  the nucleation process occurs close to

the center of the cell; see Fig. 1, since only for a small spatial regime one has  $\rho(x = L/2, y = L/2, t) \approx \rho_{\text{form}}^*$ .

To obtain the density  $\rho(x, y, t)$  from the simulation results the projection is used of the three-dimensional deposited particle distribution onto the surface plane  $P(i_x, i_y)$ . If the position  $(i_x, i_y)$  is occupied by a deposited particle we choose  $P(i_x, i_y) = 1$ , otherwise  $P(i_x, i_y) = 0$ . The density  $\rho(i_x, i_y)$  is then defined as the ensemble average of  $P(i_x, i_y)$ , i.e.

$$\rho(i_x, i_y) = \langle P(i_x, i_y) \rangle. \quad (5)$$

#### IV.2. Flux-dependence of the critical density

On a theoretical basis one can estimate the flux-dependence of the critical density  $\rho_{\text{form}}^*$ . According to mean-field nucleation theory the local nucleation rate scales like  $\Gamma_{\text{loc}} \propto \rho^{I+1}$  if  $I$  denotes the critical nucleus size. Note that in Eq. 3 the spatial dependence is given by  $x/L$  and  $y/L$ , respectively. As a consequence, the spatial range close to the center the maximum of the density distribution, where cluster formation is most likely, i.e.  $\rho_{\text{stat}}(x, y) \approx \rho_{\text{form}}^*$ , is proportional to the total area  $L^2$ . Thus, for the interesting parameter set with  $\langle N \rangle = 1$  one obtains for the total nucleation rate

$$\Gamma_{\text{tot}} \propto \rho_{\text{form}}^{*I+1}(F)L^2. \quad (6)$$

The possible flux-dependence is explicitly indicated. This relation only holds under the condition that no nucleation has occurred so far.

The nucleation rate in this case ( $\langle N \rangle = 1$ ) does not depend on the flux, as will be shown in the next Sect. V. As an immediate consequence one has the simple scaling  $\Gamma_{\text{tot}} \propto F$ , i.e. when doubling the flux and appropriately modifying the length  $L$  to keep  $\langle N \rangle = 1$  also the total nucleation rate will become twice as large. From Eq. 4 it follows that there is a direct relation between the chosen length scale  $L$  and the flux  $F$ . Choosing  $L^2 \propto \rho_{\text{form}}^*(F)/F$  one explicitly keeps track of the flux dependence in order to keep  $\rho^* \equiv \rho_{\text{stat}}$  constant. Inserting both relations into Eq. 6 one gets  $F \propto \rho_{\text{form}}^{*I+2}(F)/F$  and thus

$$\rho_{\text{form}}^*(F) \propto F^p \quad (7)$$

with  $p = 2/(I+2)$  as an immediate consequence one can predict how one has to vary the grid size  $L$  in order to keep  $\langle N \rangle = 1$  when varying the flux. In general Eq. 4 yields  $L^2 F \propto \rho_{\text{form}}^*(F)$ . Together with Eq. 7 this yields

$$L \propto F^{-q} \quad (8)$$

with

$$q = \frac{1-p}{2} = \frac{I}{2(I+2)}. \quad (9)$$

As a matter of fact we end up with the same scaling expression given by Rangelov *et al.* [27], who used a

related one-dimensional approach to analyse the island creation on stepped surfaces. The resulting scaling exponent of  $q = I/(2(I + 2))$  is in accordance with island density scaling, one would expect on a homogeneous substrate for complete condensation [16].

## V. GROWTH OF CLUSTER - QUALITATIVE BEHAVIOR

The observable  $\langle N \rangle$  is chosen to characterize the structures on substrate with adsorbing grid pre-patterns. For very small values of  $L$ , in comparison to  $L$  with  $\langle N \rangle = 1$  and fixed  $D/F$ , most particles are adsorbed at the pre-pattern boundaries and no cluster are formed in the center of the cell. In contrast, for very large  $L$  the boundary only plays a minor role and mean-field nucleation behavior can be observed [3, chap. 2]. Of particular interest is the intermediate value of  $L$  for which  $\langle N \rangle$  is unity, i.e on average a single cluster is formed *per* cell. In practice the chosen flux is tuned for a fixed  $L$ , until  $\langle N \rangle \approx 1$ .

TABLE I. Data for  $\langle N \rangle \approx 1$  with cell size  $L$ , the corresponding flux  $F$ , the average cluster number *per* cell  $\langle N \rangle$  (sum of all clusters found in 2000 cells divided by the number of cells, here 2000), the standard deviation  $\sigma$  of the distribution of clusters per cell and yield (fraction of cells with exactly one cluster).

$L/a$	$F$ in $10^{-6}/(a^2\Delta t)$	$\langle N \rangle$	$\sigma$	yield in %
40	36.11	1.026	0.208	95.6
60	12.03	1.014	0.215	95.4
80	5.85	1.004	0.212	95.7
120	2.14	1.011	0.219	95.2
160	1.08	1.006	0.212	95.5

The value of  $\langle N \rangle$  depends on the coverage of the surface. In Fig. 5 (top) the diagram  $\langle N \rangle$  against the coverage in monolayer (ML number of particles *per* full surface coverage) is shown for different values of  $L$ . The respective values for the corresponding flux are listed in Table I. Interestingly, when expressing the time in terms of the coverage, one observes no major dependence on the cell size or the flux, respectively. As a consequence, the doubling of the flux gives rise to a doubling of the nucleation rate under the condition of an appropriate choice of the new  $L$  to guarantee  $\langle N \rangle = 1$ .

The exponential fit, also shown in Fig. 5 (top), works well for a coverage larger than 0.2 ML. In this regime the nucleation rate is independent of time. Note that in the long-time regime for a coverage over 1.5 ML the value of  $\langle N \rangle$  reaches a plateau, i.e. almost no new clusters are formed. Of course, in this regime the existing individual clusters are still growing. As a consequence, the value of  $\langle N \rangle$ , determined for a coverage of 2.0 ML, is very well defined and insensitive on the chosen coverage. The exponential fit does not work for low coverage. A detailed analysis of the short-time behavior, however, is beyond the scope of this work.

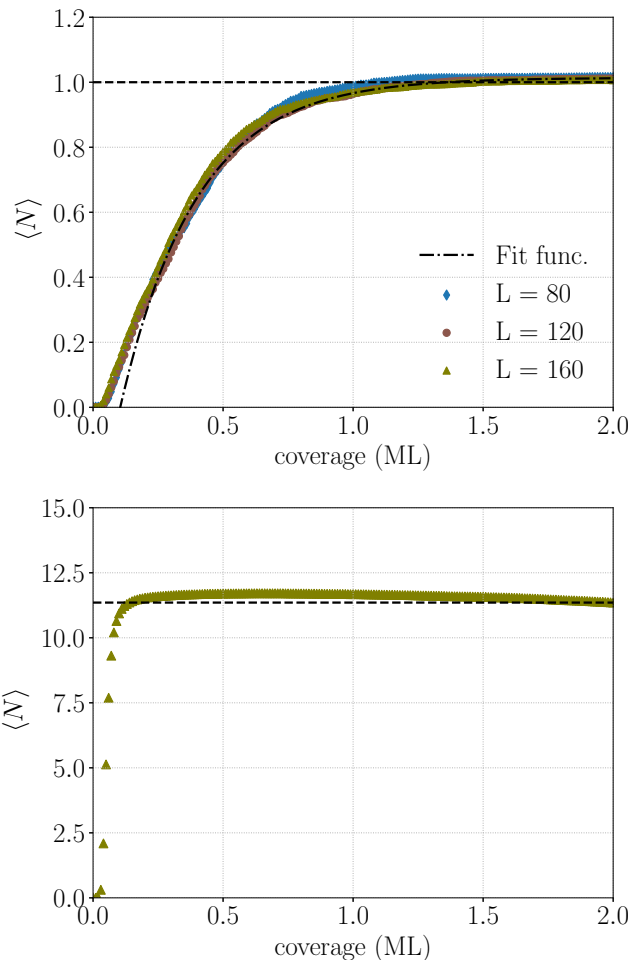


FIG. 5. Average number of clusters in dependence of the coverage. **Top:** Different  $L$  values in the case where  $\langle N \rangle$  approaches one. The respective values for the corresponding flux are listed in Table I. For  $L = 120$  an exponential fit of the form  $f(x) = c_0 - c_1 \exp(-c_2 x)$  to the long-time behavior is included. The dashed line marks  $\langle N \rangle = 1$ . **Bottom:**  $\langle N \rangle$  on grid lattice size of  $L = 160$  and flux of  $F = 5.85 \times 10^{-6}/(a^2\Delta t)$ . The dashed line marks  $\langle N \rangle = 11.4$  reached after the deposition of 2.0 ML.

In contrast, for  $F = 5.85 \times 10^{-6}/(a^2\Delta t)$  and  $L = 160$  on average more than 11 clusters are created *per* cell; see Fig. 5 (bottom). Almost all nucleation proceeds before 0.1 ML are deposited. The curve displays a maximum at 0.4 ML and slightly decreases for longer times, indicating some coarsening effect which, however is small. Therefore  $\langle N \rangle$  after the deposition of 2.0 ML is chosen to characterize the formation.

## VI. NUCLEATION AND POSITION CONTROL

One goal is to generate a structure where ideally in every cell there is exactly one cluster which, furthermore, is located directly in the center of the cell. In this scenario one might speak of ideal nucleation and position

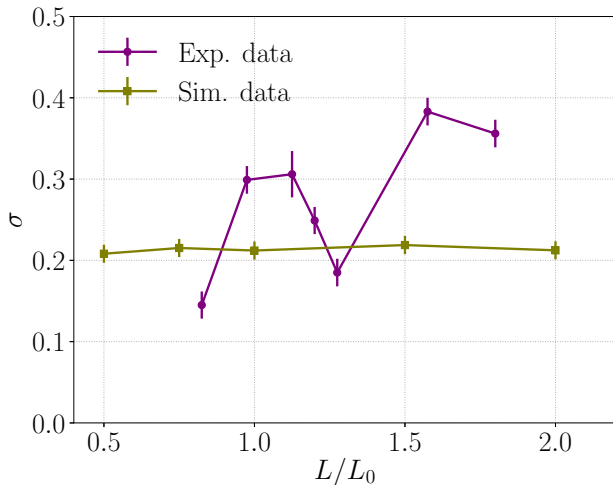


FIG. 6. Standard deviation of  $\langle N \rangle$  from experiment and simulation, for simulation data  $L_0 = 80a$  was used and for the experimental data  $L_0 = 8/3 \mu\text{m}$ . The simulation data is also listed in Table I. The errorbars are estimated with  $1/(2\sqrt{n})$ , with  $n$  as the size of the data set.

control, respectively. This implies the choice  $\langle N \rangle \approx 1$ . The opposite implication is not correct. A system with  $\langle N \rangle \approx 1$  may fail to show reasonable nucleation control, e.g. by having many cells with zero and two nuclei. In the following, the nucleation and position control from the simulations are compared with those from the experiments. First, to check the quality of nucleation, the standard deviation of the distribution of nuclei per cell is determined. The result is shown in Fig. 6. It turns out that the quality of the nucleation control from the simulations is independent of the chosen  $(F, L)$ -pair. A standard deviation of 0.2 together with an average value of unity ( $\langle N \rangle \approx 1$ ) means that in approx. 95% of all cells there is a single cluster, as listed in Table I, whereas in the remaining cells there is the same number of cells with no or two clusters. The independence from  $L$  just reflects the scaling properties, discussed above. Thus, after rescaling the time- and length scale the nucleation behavior is basically identical.

It is very promising that the standard deviations, seen experimentally, are very close to the simulated ones. This shows that the lattice model represents the key properties of the nucleation behavior, including that of the actual molecules in the experiment. The fluctuations as a function of  $L$  are much larger than expected from statistical reasons. Experimentally, reasons for fluctuation of experimental data could be related to a slightly uncontrolled coverage and contamination on the substrate.

Second, to analyse the position control we identify for each cluster the center of mass and then analyse the spatial distribution of these centers. This distribution has its maximum in the middle of the cell. In the next step we determine the full width at half maximum (FWHM). Due to the scaling arguments, already discussed above, we expect that this width should scale with  $L$ . As shown

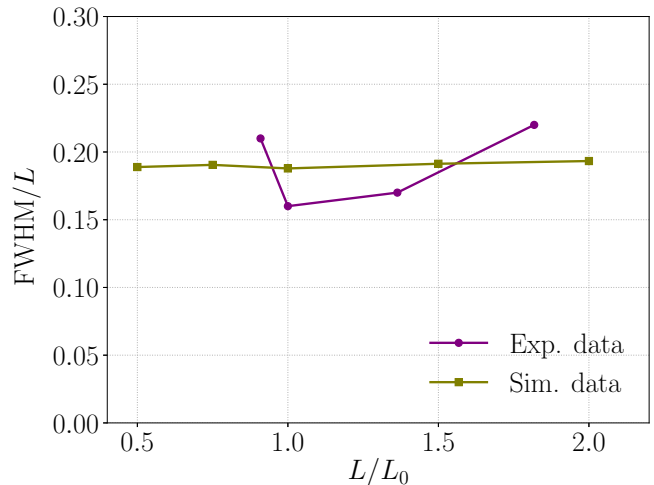


FIG. 7. Full width at half maximum of the center of mass distribution corresponding to the center of the cell  $(L/2, L/2)$  scaled by the cell size  $L$  versus  $L$ . The scaling factor  $L_0$  is the same as in Fig. 6

in Fig. 7, the ratio  $\text{FWHM}/L$  is independent of  $L$ . Again, simulations and experiments basically displays the same values. Furthermore this ratio is small which is a quantitative confirmation that not only nucleation control but also position control works very well.

At last, we looked at the average cluster sizes  $\langle s \rangle$  and the relative width of the cluster size distributions  $\omega_s$  in two and three dimensions, see Table II. By consideration of the average 2D (size of 2D projection, see Sect. IV.1) and 3D (number of particles) sizes, structural changes can be identified. These changes are expected in kinetically driven processes. In general, one would expect a scaling with  $L^2$ . Interestingly, the data in Table II shows a weaker increase. The 3D size scales with  $L^{2.00-0.18}$  and the 2D size with  $L^{2.00-0.68}$ . The strong deviations for the 2D size from a quadratic scaling can be qualitatively related to the observation that the form of the cluster changes with the external flux. For high flux (small  $L$ ) the cluster is relatively flat whereas for low flux (large  $L$ ) it starts to become more compact, displaying a more spherical shape. For lower flux the system has more time to approach the free energy minimum. Interestingly, the relative width of the size distributions in 3D and 2D is almost  $L$  independent.

TABLE II. Average cluster size in 3D (number of particles), 2D (size of 2D projection, see Sect. IV.1) and the relative widths  $\omega_s$  of the cluster size distributions for  $\langle N \rangle \approx 1$  on different grid sizes  $L$ .

$L/a$	40	60	80	120	160
3D: $\langle s \rangle$	835	1655	2844	5795	9917
3D: $\omega_s$	0.24	0.26	0.23	0.24	0.24
2D: $\langle s \rangle$	207	343	514	862	1276
2D: $\omega_s$	0.20	0.22	0.20	0.22	0.21

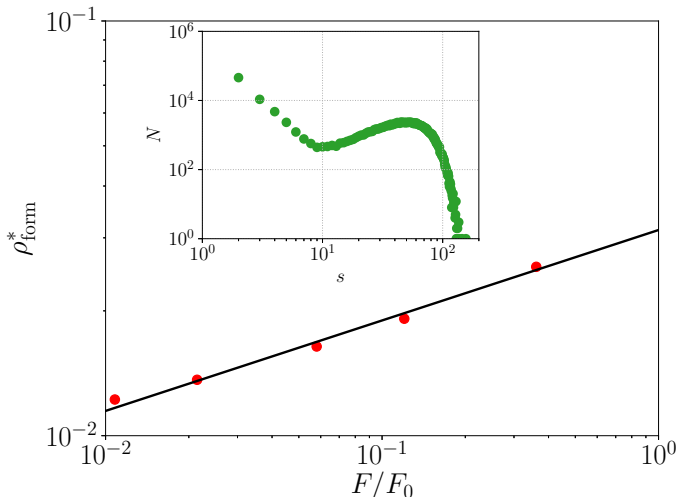


FIG. 8. Critical density  $\rho_{\text{form}}^*$  against  $F/F_0$  ( $F_0 = 10^4 \frac{1}{a^2 \Delta t}$ ) for appropriately chosen cell sizes, corresponding to  $\langle N \rangle \approx 1$ . Included is a power law fit with an exponent of  $p = 0.22$ , cf. Eq. (7). In the inset the double-logarithmic histogram of the 3D cluster sizes  $s$  is shown which is observed from simulations on un-patterned substrates. The minimum is found for a size of  $s = 9$ . The analysis is done for  $F = 12.03 \frac{1}{a^2 \Delta t}$  and a coverage of 0.1 ML.

## VII. FLUX DEPENDENCE

As discussed in Sect. IV.2 the key observable to characterize the underlying flux dependence of the cluster formation is the critical density  $\rho_{\text{form}}^*$ . Its values have been determined for different  $(F, L)$ -pairs, corresponding to  $\langle N \rangle \approx 1$  as given in Table I. For this purpose the stationary density  $\rho^*$  is determined under the condition  $\langle N \rangle \approx 1$ , like it is described in Sect. IV.1. The extracted  $\rho_{\text{form}}^*$  values are shown in Fig. 8.

As expected from Eq. 7, a power-law relation is observed between  $\rho_{\text{form}}^*$  and  $F$  with an exponent of  $p = 0.22$ . In Eq. 7 this exponent is expressed in terms of the critical cluster size  $I$ . The value of  $I$  is estimated by analyzing the distribution of cluster sizes for a simulation on an homogeneous (un-patterned) substrate. The minimum can be taken as a measure for  $I$  [40]. In this way  $I = 9$  is obtained. According to Eq. 7 this would give rise to an exponent of 0.18 which is close to the observed value of 0.22.

In the next step the dependence of the system size on the flux is predicted. As discussed in Sect IV.2 the slope should be given by  $q = (1 - p)/2 = 0.39$ . The simulated data can be described very well by this exponent, see Fig. 9 top. Using  $I = 9$ , one would end up with an exponent of 0.41, which is also very close to observed slope.

In the similar plot for the experimental  $L(F)$ -dependence, presented in Fig. 9 bottom, an exponent of  $q \approx 0.5$  is obtained under the assumption of the scaling as in Eq. 8, which is only valid for the complete condensation regime. In this case,  $q \approx 0.5$  corresponds to

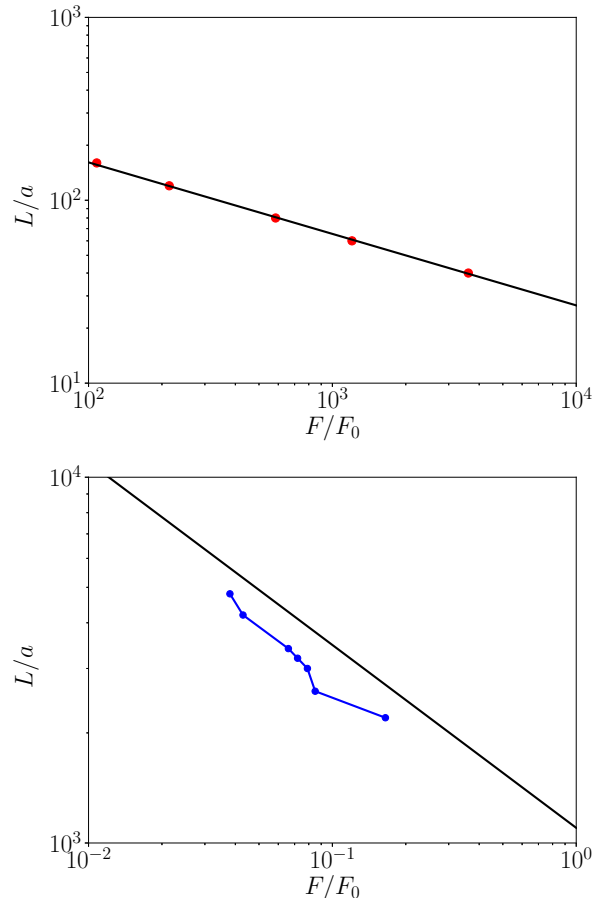


FIG. 9. Double-logarithmic representation of  $L/a$  against  $F/F_0$  for  $\langle N \rangle = 1$ . **Top:** Simulation data, included is a power law graph with an exponent of  $q = 0.39$  and  $F_0 = 10^8 / (a^2 \Delta t)$ . **Bottom:** Experimental data with  $F_0 = 1.0 \text{ nm min}^{-1}$ . In this case the value of  $L$  is expressed in units of the elementary length scale of the organic molecule which it approximated as  $a = 1 \text{ nm}$ . Included is a power-law with exponent  $q = 0.5$ .

a very large critical cluster size  $I$ . But, due to the fact of unknown condensation mechanism in the experiment, which determines the scaling of  $L(F)$  [16], we cannot determine the exact critical cluster size. Nonetheless this shows that the scaling in general is not limited to a specific regime of condensation.

## VIII. SCALING BEYOND $\langle N \rangle = 1$

### VIII.1. $F/D$ -scaling

It is known from mean-field nucleation theory that the number of clusters in the stationary long time limit on a plain substrate is a function of  $F/D$  [3, chap. 2]. In the present case this would correspond to the limit of large  $\langle N \rangle$  where the influence of the boundaries hardly matter. From our theoretical approach to nucleation control (Eq. 4) we also expect a perfect  $F/D$  scaling for  $\langle N \rangle = 1$ .

Here, this scaling with  $F/D$  is verified whether it holds

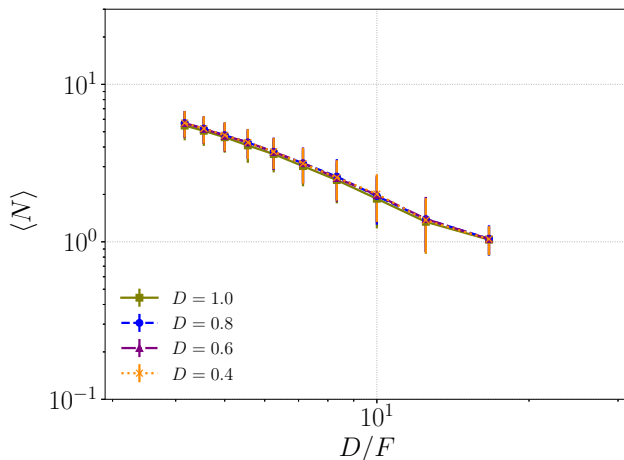


FIG. 10. Average number of clusters versus  $D/F$  for different values of the diffusion parameter as indicated in the figure and the corresponding flux  $F$  on a cell of size  $L = 80a$  in a double-logarithmic representation. The flux is scaled by factor  $10^4 a^2 \Delta t$ .

for the large range of  $\langle N \rangle$ -values. For this purpose the values of  $D$  and  $F$  are varied individually. Specifically, a diffusion parameter  $D$  is introduced as the probability to make a MC move. Therefore  $D \in [0, 1]$  for  $D = 1.0$  the KMC dynamic is as before, for  $D = 0.5$  on average every second try for a MC step is denied, for  $D = 0.0$  the system does not move at all. Thus, for decreasing  $D$  the dynamics in the system is slowed down. In Fig. 10 the average number of stable clusters  $\langle N \rangle$  is displayed against  $D/F$ . Note that a perfect scaling is observed for all values of  $\langle N \rangle$ . As a practical consequence,  $D = 1.0$  can always be chosen in order to optimize the efficiency of the MC simulations but nevertheless it covers all possible diffusion constants.

### VIII.2. Impact of length $L$

Finally, the scaling of  $\langle N \rangle$  is discussed for a fixed flux  $F = 5.85 \times 10^{-6}/(a^2 \Delta t)$  and different cell sizes  $L$  following the experimental results in Fig. 1. The data is shown in Fig. 11. Is it possible to judge from which system size the boundary conditions only have a minor impact on the nucleation behavior? Without pre-patterning one would expect the simple scaling  $\langle N \rangle \propto L^2$ . For fixed flux values we show the relation between  $\langle N \rangle$  and  $L$  in the inset of Fig. 11, both for the simulation and the experimental data. Interestingly, both data sets display a similar slope in the double logarithmic representation. It is, however, larger than two. These deviations from the expected quadratic scaling on the un-pattern substrate have their origin in the limited spatial region where nucleation can occur. This area, denoted as  $A_{\text{eff}}$ , is determined via the condition that the particle density of the overall ensemble after the deposition of 2 ML is higher than  $0.1 1/a^2$ . Plotting  $\langle N \rangle$  as a function of  $A_{\text{eff}}$  yields

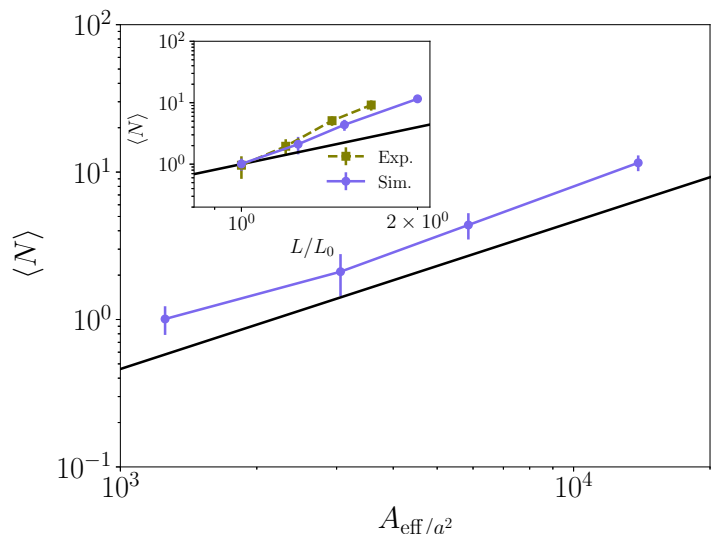


FIG. 11. Cluster number scaling against the effective nucleation area for a fixed flux  $F = 5.85 \times 10^{-6}/(a^2 \Delta t)$ . The solid line is marking a power law with a slope of one. In the inset the number of clusters is plotted as function of  $L/L_0$  ( $L_0 = 4.2 \mu\text{m}$  or  $L_0 = 80a$ ) in the double-logarithmic representation. The error bars represent the standard deviation. The solid line represents a power law with a slope of two.

a slope of one. Thus, the number of clusters is extensive and the boundary effect is reflected by the presence of a zone where no nucleation can take place.

## IX. CONCLUSIONS

Based on a new experimental way to generate a regular array of clusters, possibly formed by functionalized organic molecules, we have studied this boundary-induced nucleation control from a theoretical perspective. In particular the experimental data is compared with the outcome from kinetic Monte Carlo simulations. More specifically, the quality of nucleation and position control, the flux vs. length-dependence to guarantee the presence of a single cluster *per* cell and the dependence of the number of clusters on the effective growth area are analyzed. In all cases a very good agreement is obtained between analytical description, simulation and experiment.

Furthermore, *via* comparison with analytical expressions for the stationary concentration profile in the *cluster-free sub-ensemble* and employing key results of mean-field nucleation theory, the flux *versus* length-dependence can be fully understood. Most properties result from general scaling relations. One key result is the proportionality of the nucleation rate to the external flux under the condition that  $\langle N \rangle = 1$ . This scaling behavior was the major ingredient to connect the analytical and the numerical/experimental pieces of information. Due to the agreement of independent approaches, we suppose this mechanism of indirect nucleation control can be generalized and applied to a wide variety of growth scenarios



and materials for structure formation on the mesoscopic scale, as long a diffusion process is present on a homogeneous substrate with adjustable sinks. For appropriately related values of the diffusivity, grid size, critical cluster size and flux boundary-induced nucleation control can be achieved experimentally. We would like to stress, that this scenario explicitly occurs in a non-equilibrium setting.

We hope that combined experimental and theoretical analysis of boundary-induced nucleation control and the

observed generality of this approach may inspire more work along this line. Possible extensions to multiple component deposition are conceivable.

## ACKNOWLEDGMENTS

This work was supported through the Transregional Collaborative Research Centre TRR 61 (projects B1 and B12) by the DFG.

- 
- [1] J. E. Mahan, *Physical Vapor Deposition of Thin Films* (JOHN WILEY & SONS INC, 2000).
- [2] D. M. Mattox, *Handbook of Phys. V. Dep. (PVD) Processing* (William Andrew Publishing, 2010).
- [3] T. Michely and J. Krug, *Islands, Mounds and Atoms* (Springer-Verlag Berlin Heidelberg, 2004).
- [4] J. Evans, P. Thiel, and M. Bartelt, *Surf. Sci. Rep.* **61**, 1 (2006).
- [5] X. Niu, R. Vardavas, R. E. Caffisch, and C. Ratsch, *Phys. Rev. B* **74**, 193403 (2006).
- [6] L. Nurminen, A. Kuronen, and K. Kaski, *Phys. Rev. B* **63**, 035407 (2000).
- [7] C. Lee and A.-L. Barabási, *Appl. Phys. Lett.* **73**, 2651 (1998).
- [8] W. C. Wang, D. Y. Zhong, J. Zhu, F. Kalischewski, R. F. Dou, K. Wedeking, Y. Wang, A. Heuer, H. Fuchs, G. Erker, and L. F. Chi, *Phys. Rev. Lett.* **98**, 225504 (2007).
- [9] F. Kalischewski, J. Zhu, and A. Heuer, *Phys. Rev. B* **78**, 155401 (2008).
- [10] H. Hu, H. J. Gao, and F. Liu, *Phys. Rev. Lett.* **101**, 216102 (2008).
- [11] A. K. Engstfeld, H. E. Hoster, R. J. Behm, L. D. Roelofs, X. Liu, C.-Z. Wang, Y. Han, and J. W. Evans, *Phys. Rev. B* **86**, 085442 (2012).
- [12] A. T. N'Diaye, S. Bleikamp, P. J. Feibelman, and T. Michely, *Phys. Rev. Lett.* **97**, 215501 (2006).
- [13] J. Gadzuk, in *Dynamics*, Handbook of Surface Science, edited by E. Hasselbrink and B. Lundqvist (Elsevier, 2008).
- [14] A. Kleyn, in *Dynamics*, Handbook of Surface Science, edited by E. Hasselbrink and B. Lundqvist (Elsevier, 2008).
- [15] J. A. Venables, *Philos. Mag.* **27**, 697 (1973).
- [16] J. A. Venables, G. D. T. Spiller, and M. Hanbucken, *Rep. Prog. Phys.* **47**, 399 (1984).
- [17] M. Kotrla, *Comput. Phys. Commun.* **97**, 82 (1996).
- [18] A. C. Levi and M. Kotrla, *J. Phys.- Condens. Mat.* **9**, 299 (1997).
- [19] H. Jónsson, *Annu. Rev. Phys. Chem.* **51**, 623 (2000), PMID: 11031295.
- [20] A. Voter, in *Radiation Effects in Solids*, NATO Science Series, Vol. 235, edited by K. Sickafus, E. Kotomin, and B. Uberuaga (Springer Netherlands, 2007) pp. 1–23.
- [21] M. Petersen, C. Ratsch, R. E. Caffisch, and A. Zangwill, *Phys. Rev. E* **64**, 061602 (2001).
- [22] C. Ratsch, M. F. Gyure, R. E. Caffisch, F. Gibou, M. Petersen, M. Kang, J. Garcia, and D. D. Vvedensky, *Phys. Rev. B* **65**, 195403 (2002).
- [23] Y.-M. Yu and B.-G. Liu, *Phys. Rev. E* **69**, 021601 (2004).
- [24] M. Li, M. C. Bartelt, and J. W. Evans, *Phys. Rev. B* **68**, 121401 (2003).
- [25] G. Russo, L. M. Sander, and P. Smereka, *Phys. Rev. B* **69**, 121406 (2004).
- [26] H. Wang, O. Buller, W. Wang, A. Heuer, D. Zhang, H. Fuchs, and L. Chi, *New J. Phys.* **18**, 053006 (2016).
- [27] B. Ranguelov, M. S. Altman, and I. Markov, *Phys. Rev. B* **75**, 245419 (2007).
- [28] S. R. Forrest, *Chem. Rev.* **97**, 1793 (1997).
- [29] A. L. Briseno, J. Aizenberg, Y.-J. Han, R. A. Penkala, H. Moon, A. J. Lovinger, C. Kloc, and Z. Bao, *J. Am. Chem. Soc.* **127**, 12164 (2005).
- [30] V. C. Sundar, J. Zaumseil, V. Podzorov, E. Menard, R. L. Willett, T. Someya, M. E. Gershenson, and J. A. Rogers, *Science* **303**, 1644 (2004).
- [31] B. Lucas, T. Trigaud, and C. Videlot-Ackermann, *Polym. Int.* **61**, 374 (2012).
- [32] E. W. Forsythe, D. C. Morton, C. W. Tang, and Y. Gao, *App. Phys. Lett.* **73**, 1457 (1998).
- [33] M. Biehl, “Lattice gas models and kinetic monte carlo simulations of epitaxial growth,” in *Multiscale Modeling in Epitaxial Growth*, edited by A. Voigt (Birkhäuser Basel, Basel, 2005) pp. 3–18.
- [34] M. Strobel, K.-H. Heinig, and W. Möller, *Phys. Rev. B* **64**, 245422 (2001).
- [35] T. Müller, K.-H. Heinig, and B. Schmidt, *Mater. Sci. Eng. C* **19**, 209 (2002).
- [36] N. Metropolis, A. W. Rosenbluth, M. N. Rosenbluth, A. H. Teller, and E. Teller, *J. Chem. Phys.* **21**, 1087 (1953).
- [37] W. Tewes, O. Buller, A. Heuer, U. Thiele, and S. V. Gurevich, *J. Chem. Phys.* **146**, 094704 (2017).
- [38] W. K. Burton, N. Cabrera, and F. C. Frank, *Philos. T. Roy. Soc. A* **243**, 299 (1951).
- [39] A. K. Myers-Beaghton and D. D. Vvedensky, *Phys. Rev. A* **44**, 2457 (1991).
- [40] J. G. Amar and F. Family, *Phys. Rev. Lett.* **74**, 2066 (1995).